Spacer Switched Two Dimensional Tin Bromide Perovskites Leading to Ambient Stable Near Unity Photoluminescence Quantum Yield

Arnab Mandal,[1] Samrat Roy,[2] Anamika Mondal,[1] Shresth Gupta,[1] Bipul Pal,[2] Sayan Bhattacharyya[1]*

[1]*Department of Chemical Sciences and Centre for Advanced Functional Materials, Indian Institute of Science Education and Research (IISER) Kolkata, Mohanpur - 741246, India*
[2]*Department of Physical Sciences, Indian Institute of Science Education and Research (IISER) Kolkata, Mohanpur - 741246, India*

*Email for correspondence: sayanb@iiserkol.ac.in

Abstract

Semiconductor nanostructures with near-unity photoluminescence quantum yields (PLQYs) are imperative for light-emitting diodes and display devices.A PLQY of 99.7±0.3% has been obtained by stabilizing 91% of the Sn^{2+} state in the Dion-Jacobson (8N8)$SnBr_4$ (8N8-DJ) perovskite with 1,8 diaminooctane (8N8) interlayer spacer. The PLQY is favoredby a longerchain length of the hydrophobic spacer molecule, the extent of octahedral tilting and the preference of Sn^{2+}at the*B*-site over Pb^{2+}.The near-unity PLQY of 8N8-DJ has outstanding ambient stability under relative humidity (RH) of 55%for30 days throughout the entire excitation wavelength range, RH 75% for 3 days and 100°C for 3 h. By changing the spacer to *n*-octylamine (8N), Ruddlesden-Popper $(8N)_2SnBr_4$ (8N-RP) also has an appreciable PLQY of 91.7±0.6%, but having poor ambientstability due to increased lattice strain and structural degradation. The PL experiments from 5K to 300K decipher the room temperature PLQY to be due to the self-trapped excitons (STE) where the self-trapping depth is 25.6±0.4 meV below the conduction band as a result of strong carrier-phonon coupling. With 34.7-37.3meV exciton binding energy, the ~5.5 μs long-lived STE emission dominates over the band edge (BE) peaks at lower excitation wavelengths and higher temperatures. The higher PLQY and stability of 8N8-DJ are due to the stronger interaction between $SnBr_6^{4-}$ octahedra and 1,8 diammonium octane cation leading to a more rigid structure. The near-unity PLQY of 8N8-DJ also remains unchanged from its powder form to the polymer-embedded perovskite films.

*Keywords:*Lead-free 2D perovskite; Photoluminescence quantum yield; Self-trapped emission; PLQY stability; carrier-phonon coupling

Introduction

Metal-halide perovskite is one of the disruptive class of materials because of their potential application in optoelectronics and photovoltaics,[1-4] particularly so, when they are prepared with minimal structural disorder, high thermal resistance and photo-stability. Solution-processed all-inorganic $CsPbX_3$ (X = Cl, Br, I) nanocrystals (NCs) have reached 100% PLQY due to the synthetic marvels that resulted in a substantial reduction of the non-radiative recombination centers and trap-mediated non-radiative losses.[5]Such a high PLQY can be sustained by maintaining the phase stability of these NCs under ambient conditions, which is an arduous task. Two-dimensional (2D) perovskites have emerged as next-generation systems with better moisture and heat stability.[6] Among them, the Ruddlesden-Popper (RP) and Dion-Jacobson (DJ) phases are most common, denoted by the formula $A'_2A_{n-1}M_nX_{3n+1}$, and $A''A_{n-1}M_nX_{3n+1}$, respectively, where A′ is a monovalent and A″ is a bivalent interlayer spacer cation, A is a smaller monovalent cation (MA^+, FA^+ or Cs^+), M is a divalent metal (Pb^{2+} or Sn^{2+}) and X is Cl^-, Br^- or I^-.The A′ and A″ hydrophobic alkyl ammonium chains render stability to the 2D perovskites and act as a barrier in between the MX_6^{4-} octahedral layers forming a quantum well-like structure by increasing the potential barrier. Blessed with a strong quantum confinement by the bulky spacer cations, RP and DJ perovskites have shown decent PLQY.[7-10]However, a gap area persists since the ambient stability of PLQY is rarely explored or the origin of PL emission being seldom explained in Sn-based 2D perovskites.The PL stability can be rendered by *B*-site doping,[10] using modified RP structures,[11]or by antisolvent processing, etc.[12]

The RP phase, $PEA_2Cs_{2.4}MA_{0.6}Pb_4Br_{13}$ (PEA: phenylethylammonium; MA: methylammonium) capped with triphenylphosphine oxide has demonstrated 97% PLQY.[7]The Pb-free RP perovskites such as $(C_{18}H_{35}NH_3)_2SnBr_4$ and $(C_8H_{17}NH_3)_2SnBr_4$ have 88 and 98% PLQY, respectively.[8,9]There are only a few DJ perovskites with appreciable PL emission, where 88% quantum yield in $ODASnBr_4$ (ODA: protonated 1,8-octanediamine) is a rare observation.[13]The RP and DJ phases offer the advantages of a tunable electronic structure depending on the number of layers (*n*),[14] decent luminescence by the confinement of excitons within the potential barrier,[15] and stabilization of the labile oxidation states by the hydrophobic organic spacer.[16]However, the RP phases lack the potential in optoelectronics because of the insulating gap between two layers of the protonated ligands held together by van der Waals

interactions.[17]The DJ perovskites are benefitted by H-bonding between the divalent organic cation and the inorganic perovskite octahedra at both ends, thereby rendering better structural stability,[18]for their potential use in optoelectronic devices.[19,20]

Based on this logic, we have changed the interlayer ammonium spacer from *n*-octylamine (8N) to 1,8 diaminooctane (8N8) to synthesize $(8N)_2SnBr_4$ (8N-RP) with PLQY of 91.7±0.6%and $(8N8)SnBr_4$ (8N8-DJ) with near-unity PLQY of 99.7±0.3%. Both these perovskite phases were prepared by acid precipitation at 100°C with high reproducibility and yield. The structural stability of the RP and DJ phases is expected to contribute to the sustainability of the PL emission and the quantum yield even after prolonged exposure to the ambient atmosphere. Only the DJ phase with lower lattice strain retains its excitation wavelength (λ_{ex}) dependent PLQY for over a month under RH of 55%.Sn^{2+} has a comparable ionic radius to Pb^{2+} (r_{Sn2+} = 1.15 Å; r_{Pb2+} = 1.19 Å) and similar ns^2 outer electronic configuration.[21]In fact, the 3D tin halide perovskites have shown narrower optical bandgap, higher electron mobility >2000 $cm^2\ V^{-1}\ s^{-1}$ and hole mobility >300 $cm^2\ V^{-1}\ s^{-1}$.[22]In our case, the Sn^{2+} state is better stabilized in 8N8-DJ. The outstanding PL emission and high quantum yield is the result of STE emission at λ_{ex}< 360 nmdue to the carrier-phonon coupling mediated formation of delocalised state below the conduction band.The origin of near-unity PLQY has been elucidated by analyzing the PL spectra from 5K to 300Kas well as from a combination of higher out-of-plane octahedral tilt and elongation in the inorganic layer.We start our discussion with the 8N8-DJ system followed by its comparison toDJ perovskites with lower spacer chain lengths, 8N-RP and an analogous system with Pb^{2+} at the *B*-site.

Results and Discussions

Structural characteristics of 8N8-DJ

Figure 1aprovides a structural view of 8N8-DJ [$A''A_{n-1}M_nX_{3n+1}$, A″ = 1,8 diammonium octane (8N8), M = Sn^{2+}, X = Br^- and*n* = 1]where the inorganic $SnBr_6^{4-}$ layers are separated by a single layer of 8N8 spacer. Here, $SnBr_2$was used as the tin precursor and H_3PO_2 as thereducing agent to preserve the +2 oxidation state of Sn. The equidistant 2θ reflections in the X-ray diffraction (XRD) pattern attest to the 2D layers (Figure 1b). The interplanar distance between the inorganic layers in the monoclinic crystal structure with $P2_1/c$ space group is calculated as 13.9 Å from the (002) reflection at 2θ = 6.4° and the equidistant reflections spanning over Δ2θ = 6.4°.[8]This XRD pattern is in stark contrast to that of the 0D organic tin bromide, which usually

forms during the diffusion of dichloromethane, as the bad solvent, into N,N-dimethylformamide, as the good solvent containing the Sn precursors.[23]The 0D perovskite can be converted into the 2D form during the subsequent drying process. However, our one-step acid precipitation technique can rule out the possibility of any0D impurity.The single crystal data of 8N8-DJ matches the powder XRD pattern and affirms the purity of the sample (Figure S1). The obtained lattice parmeters of the monoclinic crystal are a = 9.74(17) Å, b = 13.65(3) Å, c = 17.98(6) Å and β = 93.2(1)°.The 1,8 diammonium octane cationhas a chain length of 11.3 Åcalculated by the formula $\sin\frac{\theta}{2} = \frac{x}{a}$, where θ is 109.5°, the angle between sp^3 hybridized carbon atoms, and a is the C-C bond distance (Figure 1c). The 8N8 chain length of 11.3 Åis very close to the interlayer distance of 13.9 Å suggesting the presence of a single divalent cation in between the $SnBr_6^{4-}$ blocks and the absence of any van der Waals interaction.[24]The 8N8-DJ sheets are in fact 16.1±2.4 nm thick due to the stacking of multiple unit cells, as observed by atomic force microscopy (AFM) in FigureS2a,b.The stacking and wide lateral spread of the 8N8-DJ sheetsis also noticed in the scanning and transmission electron microscope (SEM and TEM) images (Figure S2c.d).The Sn:Br:N atomic ratio of 1:4:2 obtained from the homogeneous elemental mapping also specifies the n = 1composition of (8N8)$SnBr_4$(Figure S3).

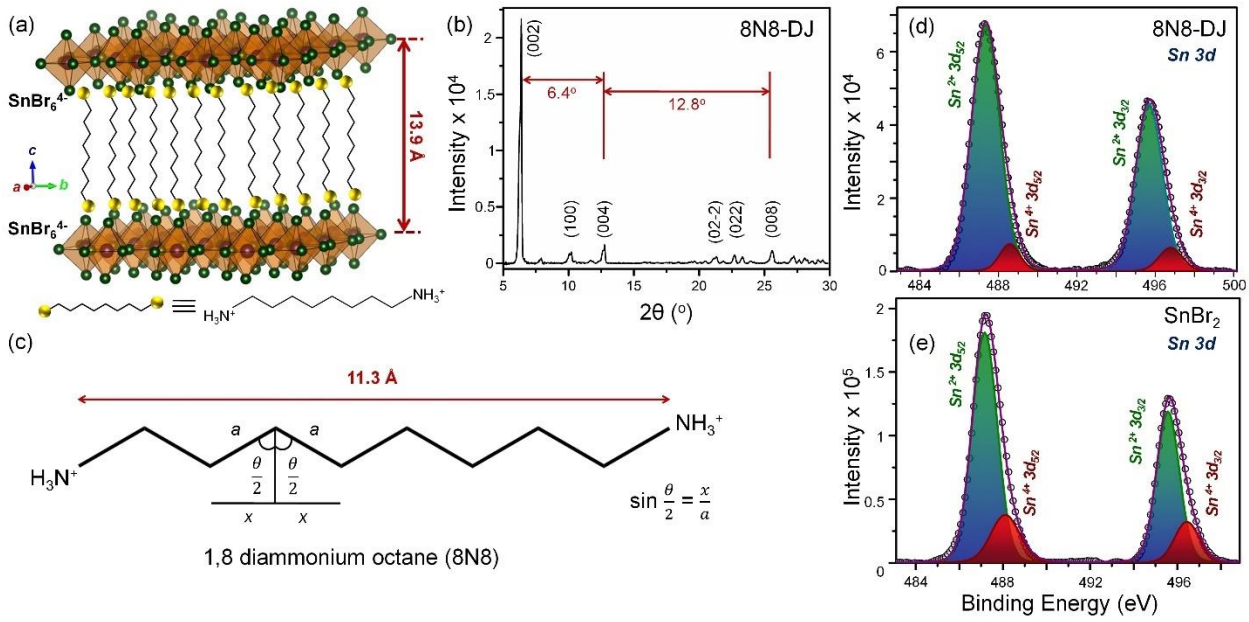

Figure 1. (a) Schematic crystal structure and (b) XRD pattern of 8N8-DJ. (c) Chain length of 1,8 diammonium octane ligand. XPS plots of Sn *3d* level in (d) 8N8-DJ and (e) $SnBr_2$.

The X-ray photoelectron spectral (XPS)data from Sn *3d* level of 8N8-DJ perovskite shows the retention of Sn^{2+} species that stabilizes the perovskite phase (Figure 1d).Because of the presence of H_3PO_2 as a reducing agent during its synthesis, 8N8-DJ has only 9 wt% Sn^{4+}much lower than 21 wt% for $SnBr_2$ (Figure 1eand Table S1). Deconvolution of the N *1s* level shows that the population of pronated amine at higher binding energy is 5-times more than the non-protonated counterpart (Figure S4).Since 8N8 spacer is primarily protonated and connects the$SnBr_6^{4-}$inorganic blocks, the C *1s* level also has C-C, C-N and C-O species. The binding energy shift of the Br *3d* level indicates the chemical interaction between the $SnBr_6^{4-}$ unit and the protonated ligand.

Optical properties of 8N8-DJ at room temperature

At room temperature, 8N8-DJ exhibits a sharp absorption bandbelow 400 nm and a broad and intense yellow emissioncentered at ~580 nm with ~130 nm full-width at half-maximum (FWHM) and Stokes shift of ~190 nm with λ_{ex} of 360 nm (Figure 2a). The perovskite powder emits orange-yellow color under365 nm UV light (Figure 2a inset).When 8N8-DJ perovskite is stored under ambient conditions of 25°C and RH of 55%, for over 30 days, its optical absorbance remains unchanged (Figure S5), and 75% of the PL intensity is retained (Figure 2b).The intense PL excitation (PLE) spectrum also exhibits ~85% retention after the 30 days storage (Figure S6).The PL intensity is dependent on λ_{ex}wherethe integrated area under the curve increases with decreasing λ_{ex}(Figure 2c). The PL stability of the 8N8-DJ perovskite has been tested by PL reversibility experiments where λ_{ex} was varied in cycles from 320 to 420 nm (Figure 2d). In such a scenario, 8N8-DJ demonstrates an immaculate stability by retaining the PL intensity undamped at each λ_{ex}.

The absolute PLQY has a striking similarity to the dependence of PL intensity on λ_{ex} (Figure 2c). An outstanding near-unity PLQY is observed in the λ_{ex} range from 320 to 350 nm(Figure 2e). At λ_{ex} = 350 nm, the PLQY is measured as 99.7±0.3%. Just like the PL emission, 8N8-DJ shows pristine PLQY stability, observed with the 30 days old sample at all λ_{ex} (Figure 2f). As discussed earlier, one of the major drawbacks of Sn-based perovskites is their unstable nature because of the self-oxidation of Sn^{2+}. In the recent times, proton donors in the form of alcohols, dichloromethane and chloroform have been used to stabilize the 2D phase and to attain an appreciable PLQY.[13,25]Acid precipitation with varying amounts ofHBr and H_3PO_2 have also

resulted in ~98% PLQY of ODASnBr$_4$ but without any confirmed stability.[26] Our trick was to use an excess of H_3PO_2 as the reducing agent that helped to stabilize the Sn^{2+} state. Even though the excess organic ligands and acids can act as impurities that further degrade the structure and hence the PLQY, we have ensured an extensive washing by ether and chloroform to remove such impurities.In our case, the sublime stabilities of PL emission and absolute PLQY is an outstanding result owing to the protection of the inorganic $SnBr_6^{4-}$blocks with 91 wt% Sn^{2+} state by the hydrophobic long-chain 1,8 diammonium octane cation.

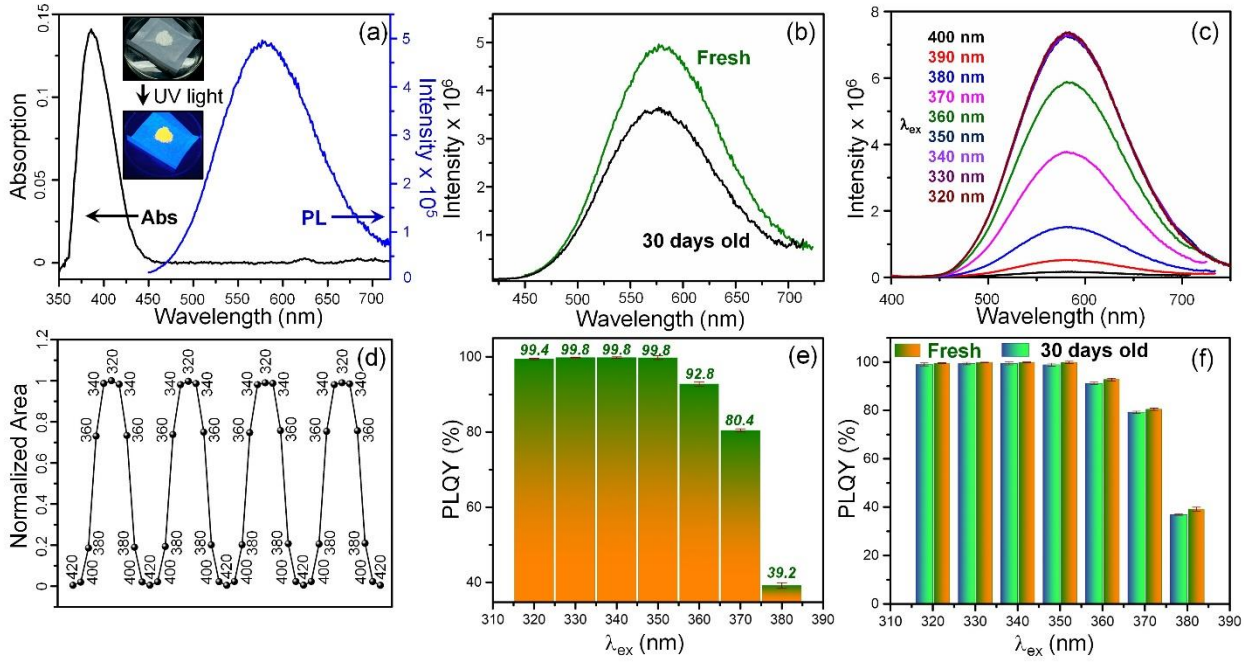

Figure 2. Room temperature optical properties of 8N8-DJ powder. (a) Absorption and PL emission spectra (λ_{ex} = 360 nm). (b) PL spectra of fresh and 30 days stored samplesunder RH of 55% at 25°C(λ_{ex} = 360 nm). (c) λ_{ex} dependent PL spectra and (d) PL intensity reversibility plot where the numbers depict λ_{ex} variation between 320 and 420 nm. (e) Bar plots of PLQY at different λ_{ex}. (f) Bar plots illustrating the ambient-stability of PLQY where the fresh and 30 days old sample are shown to have comparable bar heights at different λ_{ex}.

Although the PLQY shown in Figure 2e,fwas recordedwith the 8N8-DJ powder, optoelectronic devices need large-area films where the non-radiative recombination due to the agglomerations and pin-holes are deleterious to thelight absorption and emission.[27]Three 1 cm^2 8N8-DJ films were prepared with polymethyl methacrylate (PMMA) binder where the perovskite concentrations are 250, 125 and 83 mg/mL, and these films are termed as DJ-1, DJ-2

and DJ-3, respectively. All the 8N8-DJ-PMMAfilms exhibit yellow luminescence under 365 nm UV light(Figure S7a).The PL intensity is expectedly proportional to the increasing film thickness from DJ-3 to DJ-1 (Figure S7b; λ_{ex} = 350 nm). In spite of the adversaries of a rough polymer-embedded film, the PLQY of DJ-1 film remains almost intact at λ_{ex} = 350 nm, and is marginally altered for DJ-2 and DJ-3 films having lower film thickness in correlation to the changes in PL intensity (Figure S7c).

Origin of near-unity PLQY of 8N8-DJ

Thelow temperature PL experiments of the 8N8-DJ perovskite were performed at λ_{ex} of 360, 380 and 400 nm, using a laser probed set-up coupled to a closed cycle He cryostat to unravel the origin of the near-unity PLQY at room temperature(Figure S8).The PL measurements have been carried out under very low excitation intensities, considering the possibility of saturation of the excitonic states. The average laser power was varied in the range of 25-400 μW (Figure S9a), and the PL spectra show no sign of saturation. In fact, the PL intensities continue to increase linearly with the excitation power (Figure S9b). Similar to the continuous-wave (CW) laser excitation used in conventional PL measurements,[13,25,26] the high-repetition rate of 80 MHz pulsed excitation in our PL experiments, allow the attainment of a steady-state population density for the STE, bound and free excitons. The steady-state population density depends on the photocarrier generation rate which is essentially governed by the excitation intensity, and lifetime of the various states involved in the PL emission. The steady-state population of the excited carriers attains thermal equilibrium among themselves before their radiative relaxation via PL emission.

With λ_{ex} of 380 nm, the intensity of the yellow emission centered at ~580 nm increases with temperature from 5to 300 K, although below 100K, a distinct PL emission centered at ~440 nm is observed(Figure3a,b).This emission band is likely due to the band edge (BE) emission and the yellow emission arises from the STE, which is common in low-dimensional perovskites for emitting white light.[28] The BE emission is due to emission from the spin and parity allowed $^1P_1$ excited state to the $^1S_0$ ground state, which is common for systems with ns^2 electronic configuration, here Sn^{2+}(Figure 3c).[29,30]When the non-radiative electron capture by permanent deep trapsand electron transfer to the STE state are reducedat temperatures less than 150K, partial electron transfer can also occur from $^1P_1$ excited singlet state to the $^3P_1$ triplet state, followed by emission from $^3P_1$ to $^1S_0$.The self-trapped states are created by the overlapped

discrete energy states below the conduction band because of strong carrier-phonon coupling. STE involves the transfer of charge carriers from the conduction band to these overlapped states and emission from the self-trapped state.[31] At <100K, when the excited electrons have lower thermal energy, the carrier-phonon coupling becomes subservient which lowers the STE band intensity relative to the BE emission. With the increase of temperature, the excited electrons gain thermal energy to overcome the activation energy for their transport from the conduction band to the STE state.

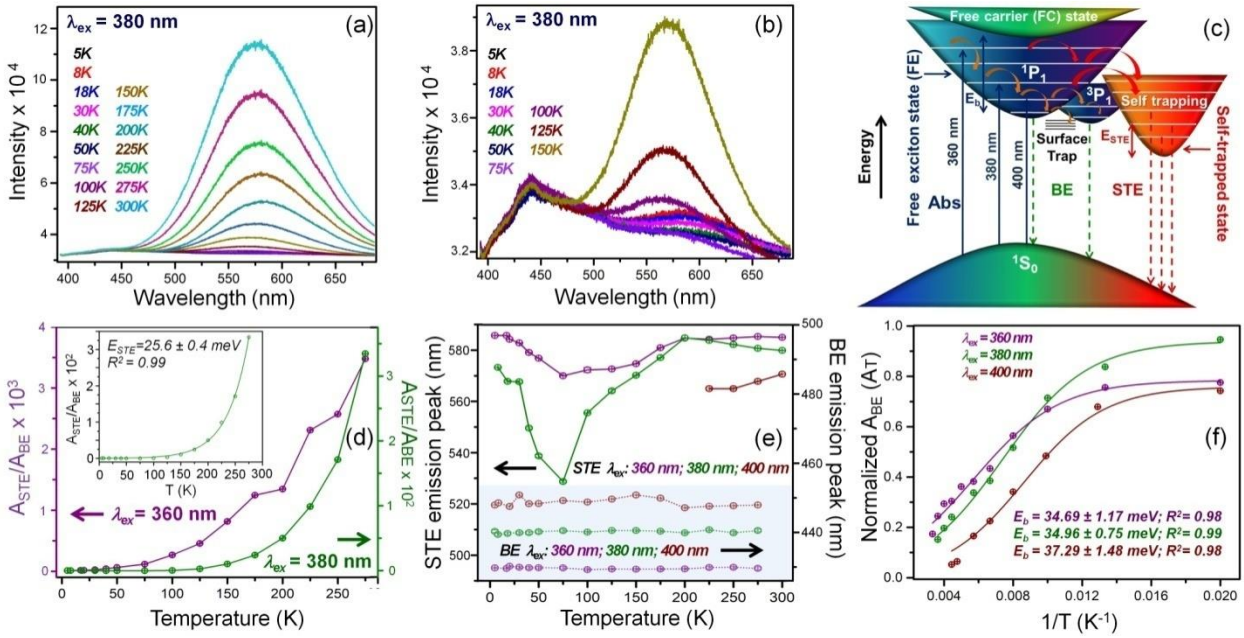

Figure 3. Temperature dependent optical properties of 8N8-DJ powder. PL spectra (a) in the range 5K to 300K and (b) the magnified view from 5K to 150K (λ_{ex} = 380 nm). (c) Schematic of the energy level diagram demonstrating the BE and STE emission. (d) Temperature variation of A_{STE}/A_{BE} ratio at λ_{ex} of 360 and 380 nm. Inset shows the fitted A_{STE}/A_{BE} vs temperature plot at λ_{ex} = 380 nm for the determination of E_{STE}. (e) Temperature variation of STE and BE peak positions and (f) the fitted plot of normalized A_{BE} vs 1/T at λ_{ex} of 360, 380 and 400 nm.

The PL experiments were also performed with different λ_{ex} at 5K (Figure S10a). The STE band presides over the BE emission at λ_{ex}< 380 nm, whereasat λ_{ex} above 380 nm only the BE peak is observed. In fact at any given temperature, the STE emission is more favorable at lower λ_{ex}, in which case the electrons could be excited to higher vibrational energy states from where the transfer of the electrons to the delocalized STE states becomes favorable (Figure 3c). Likewise, with λ_{ex} = 360 nm, the STE emission is dominant from 5 to 300K, and at λ_{ex} = 400

nm, the BE emission is in turn predominant up to 200K, above which the STE band appears with lower intensity (Figure S10b,c). Considering the integrated area (*A*)under the curve, the A_{STE}/A_{BE} ratio is greater for λ_{ex} of 360 nm than 380 nm at all temperatures (Figure 3d). At λ_{ex} of 360 nm, the A_{BE}/A_{STE} ratio expectedly shows an opposite trend except when λ_{ex} is increased to 380 nm, where the ratio increases till 50K and decreases thereafter (Figure 3b and Figure S11a). The BE emission intensity decreases at the cost of non-radiative capture of charge carriers by permanent deep trap states at higher temperatures. On the contrary, STE band intensity increases because of enhanced carrier-phonon coupling. Since STE emission is more dominant at lower λ_{ex} and the maximum PLQY is also obtained at lower λ_{ex} (Figure 2e), one can comprehend the high PLQY to be the result of intense STE emission.

The stabilization of the carriers transferred from the free exciton state (FE)to the STE stateis given bythe energy of self-trapping depth(E_{STE}) which can becalculated by fitting theArrhenius relation to the plot of A_{STE}/A_{BE}vs temperature (Figure 3c and Figure3d inset). At λ_{ex} of 380 nm, E_{STE}isestimated as 25.6±0.4 meV from the fitted curve that reaches a plateau due to reduced STE emission below 100K.The E_{STE} of 8N8-DJ is higher than other similar systems,[31]indicating a significantdetrapping energy that is required for back transfer from STE to the FE state.As shown inFigure3e, the BE emission peak position is independent of temperature at each λ_{ex}. Otherwise, the STE emission is blue shifted from 5K to 75K followed by the red shift upto 300K. The variation of the STE peak positioncan be explained by the competitive effect of thermal expansion (A_{TE}) and electron-phonon (A_{EP}) interactions according to equation (1):[32]

$$E(T) = E(0) + A_{TE}T + A_{EP}\left(\frac{2}{\exp\left[\frac{\hbar\omega}{k_B T}\right]-1} + 1\right) \quad (1)$$

where E_0 is the unrenormalized bandgap, A_{TE} and A_{EP} are the contributionsfrom TE and EP interactions, respectively, and $\hbar\omega$ is the average optical phonon energy.The STE band is blue shifted from from 5 to 75K (Figure S11b), due to the increased thermal expansion. With further increase in temperature beyond 75K the PL band is redshifted as a result of the higher extent of electron-phonon interaction.[32]Because of the thermal expansion effect, the STE band energy increases from 5K to 75K with temperature coefficient (σ) of1.04 ± 0.04 and 2.84±0.14 meVK^{-1}at$\lambda_{ex}$of 360 and 380 nm, respectively (Figure S11b,c).[33]From the variation of A_{BE} with

temperature (*T*) and 1/*T*(Figure3f and Figure S10d), the exciton binding energy (E_b) of the 8N8-DJ perovskite can becalculated by fitting the plots of Figure3f with equation (2):[13]

$$A(T) = \frac{A(0)}{1+\exp\left[-\frac{E_b}{k_B T}\right]} \quad (2)$$

where, *A(T)* and *A(0)*are the A_{BE} at T K and 0K, respectively. At λ_{ex} of 360, 380 and 400 nm, $E_b$is calculated as 34.7±1.2, 35.0±0.8and 37.3±1.5meV, respectively (Table S2). The λ_{ex} independentE_b values imply a favorableelectronic transition of the free exciton state (FE) to the free carrier state (FC) for enabling a favorable electron extraction.[34]

The extent of carrier-phonon coupling can be further understood by analyzing the FWHM of the PL emission bands (Figure S12). Although there is no appreciable temperature variation of FWHM of the BE emission bands, the FWHM of STE emission band shows a linear increase with temperature at 360 nm excitation. Otherwise, at λ_{ex} of 380 nm, the FWHM of the STE emission band initially decreases from 5 to 50K, due to the decrease of STE emission intensity in that range. Equation (3) is used to fit the temperaturedependence of FWHM (in eV) of the STE emission band:[13]

$$FWHM\ (T) = 2.36\sqrt{S}\ \hbar\omega_{ph}\sqrt{\coth\left(\frac{\hbar\omega_{ph}}{2k_B T}\right)} \quad (3)$$

where $\hbar\omega_{ph}$ is the phonon frequency, *S* is the electron-phonon coupling parameter (Huang–Rhys factor), and k_B is the Boltzmann constant. At λ_{ex} of 360 nm,*S* and $\hbar\omega_{ph}$are28.5±1.4 and 24.3±0.7 meV, respectively, higher than the corresponding values of 27.4±1.9 and 21.3±0.9 meV for 380 nm exciation(Table S3). The near-unity PLQY at $\lambda_{ex} \leq$ 360 nm is a direct reflection of the >10*S*values, suggesting a significant electron-phonon coupling.[13]The contribution of different phonon components can be explained by fitting the FWHM vs 1/T plots with equation (4):[33]

$$\Gamma(T) = \Gamma(0) + \Gamma_{ac} + \Gamma_{LO} = \Gamma(0) + \gamma_{ac} T + \gamma_{LO} n(T) = \Gamma(0) + \gamma_{ac} T + \frac{\gamma_{LO}}{\exp\left[\frac{E_{LO}}{k_B T}\right]-1} \quad (4)$$

where *Γ(T)*and *Γ(0)* are the FWHM at temperature TK and 0K, respectively. Γ_{ac} and $\Gamma_{LO,}$ are the acoustic and longitudinal optical (LO) phonon modes, γ_{ac} and γ_{LO} are the exciton-acoustic phonon coupling coefficient and exciton-LO phonon coupling strength, respectively. E_{LO} is the characteristic LO phonon energy. Similar to the Huang–Rhys factor, the greater γ_{LO} indicatesincreasedcarrier-phonon coupling at lower λ_{ex}. $\gamma_{LO}$is 195.0±1.3 and 179.0±3.2 meVat λ_{ex} of 360 and 380 nm, respectively (Table S3).

Structural and optical characteristics of DJ perovskites with different spacers

To examine the impact of the spacer chain length, the aliphatic molecule was varied from 1,8 diamino octane (8N8) to 1,6 diamino hexane (6N6) and 1,4 diamino butane (4N4) to synthesize $6N6SnBr_4$ (6N6-DJ) and $4N4SnBr_4$ (4N4-DJ), respectively.Both 6N6-DJ and 4N4-DJ perovskites have equidistant XRD peaks (Figure 4a), similar to the 8N8-DJ, although the XRD peaks are spaced farther apart from 8N8-DJ to 4N4-DJ, implying a lower interplanar distance between the inorganic layers. The interplanar distance of 4N4-DJ is 10Å, lower than 6N6-DJ (11.1 Å) and 8N8-DJ (13.9 Å). Due to a reduced quantum confinement by the smaller chain length, the absorption edge is red shifted from 8N8-DJ to 4N4-DJ (Figure 4b). There is a gradual decrease of STE emission intensity from 8N8-DJ to 4N4-DJ(Figure 4c), because of which 4N4-DJ perovskite exhibits a BE shoulder at ~480 nm along with the STE emission (Figure 4d). The PLE spectrum of 8N8-DJ has a wider wavelength spread and higher PLE intensity than 6N6-DJ and 4N4-DJ perovskites (Figure 4e), leading to a much higher PLQY (Figure 4f, recorded at the maximum λ_{ex}in the respective PLE spectra). The lowering of PLQY with decreasing chain length of the spacer molecule is directly correlated to the lower STE emission intensity.

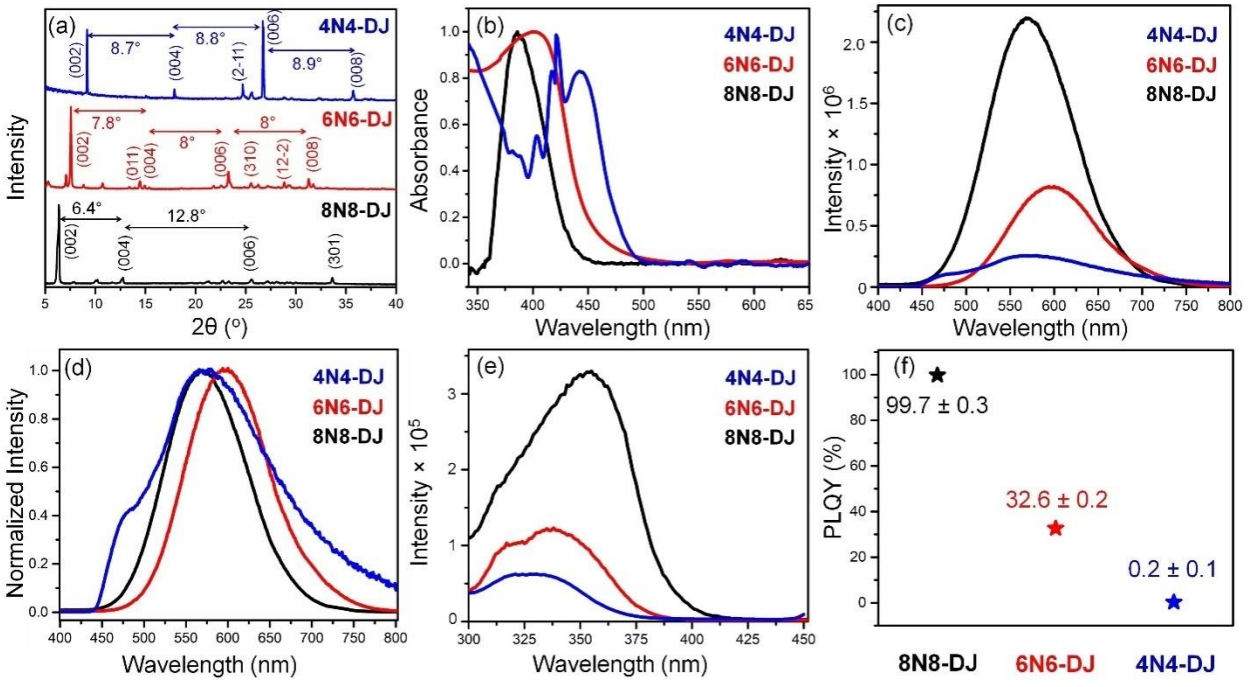

Figure 4. (a) XRD patterns, (b) optical absorption, (c, d) PL emission spectra (λ_{ex} = 360 nm), (e) PLE spectra and (f) maximum PLQY of 4N4-DJ,6N6-DJ and 8N8-DJ perovskites.

Since STE depends on the $SnBr_6^{4-}$ octahedral tilting in the inorganic layer, the STE emission intensity increases with higher out-of-plane octahedral tilting.[35] The octahedral tilting is again directly proportional to the compressive strain, which can be measured from the slopes of the Williamson-Hall plots(Figure S13a-c). 8N8-DJ has a highercompressive strain of $2.3(\pm0.1)\times10^{-3}$ than $2(\pm0.1)\times10^{-3}$ for 6N6-DJ and $1.5(\pm0.1)\times10^{-3}$ for 4N4-DJ, which causes moreout-of-plane octahedral tilting and a greater degree of STE in the former. An increase in out-of-plane octahedral tilting with the increasing spacer chain length was evaluated by using the CIF files of $8N8PbBr_4$ and $4N4PbBr_4$analogous systems (Figure S13d).[36] A greater out-of-plane octahedral tilting (148.2°) is observed for 8N8-DJ as compared to the 4N4-DJ (149.8°).

Effect of the B-site cation

In addition to the influence of spacer chain length, we also show that the PLQY of DJ perovskites strongly depends on the *B*-site cation and the extent of octahedral distortion. With our 8N8-DJ and $8N8PbBr_4$, the degree of octahedral distortion was evaluated by considering two elongation factors (λ_{oct} and σ^2) according to the equations (5) and (6):[37]

$$\lambda_{\mathrm{oct}} = 1/6 \sum_{n=1}^{6} \left[\frac{\mathrm{d_n}-\mathrm{d_0}}{\mathrm{d_0}}\right]^2 \quad (5)$$

$$\sigma^2 = 1/11 \sum_{n=0}^{12} (\theta_{\mathrm{n}} - 90^{\circ})^2 \quad (6)$$

where d_n is the six *B*-Br bond length, d_0 is the average *B*-Br bond length and θ is each Br-*B*-Br bond angle (*B* = Pb^{2+} and Sn^{2+}). 8N8-DJ has higher elongation factors, $\lambda_{oct}$of $7.1 \times 10^{-5}$and $\sigma^2$of 3.85, whereas the λ_{oct} and σ^2values of $8N8PbBr_4$ are 5.2×10^{-7} and 3.59, respectively(Figure S14a). The λ_{oct} and σ^2 were calculated from the CIF files with CCDC no. 2016173 for 8N8-DJ and 1521059 for $8N8PbBr_4$.[13,36] The larger elongation factors of 8N8-DJ lead to more octahedral distortion, which is responsible for the prominent STE emission and high PLQY. In spite of having a similar structure with equidistant 6.6° apart XRD reflections (Figure S14b), the lower elongation factors of $8N8PbBr_4$changes its emission characteristics. $8N8PbBr_4$exhibits a sharp BE emission band with lower FWHMof 32.4 ±1.2 nm and stoke's shiftof 3.7 nmwithout any fluorescence characteristics(Figure S14b,c).Therefore, 8N8-DJ has the right combination of the 8N8 spacer molecule and a stabilized Sn^{2+} cation at the *B*-site, to enable the near-unity PLQY

resulting from the strong STE emission. The results have a direct correspondence to the perovskite structure particularly the out-of-plane distortion in the $SnBr_6^{4-}$ octahedra.

Structural and optical characteristics of 8N-RP perovskite

In 8N-RP, the $SnBr_6^{4-}$ layers are separated by two layers of organic *n*-octylammonium cation, held together by van der Waals forces, making it less rigid than the 8N8-DJ system (Figure 5a). The XRD pattern contains equidistant reflections at $2\theta < 27^o$ with interplanar distance of 20.1 Å between the inorganic blocks (Figure 5b and Figure S15a). The *n*-octylammonium cation has a chain length of 10.04 Å, half the interplanar distance, validating a sandwich of two organic cations. The 35.3±3.3 nm thickness (Figure S15b,c) is due to the stacking of atomic layers over a wide lateral spread of the 8N-RP sheets (Figure S15d,e).Both 8N8-DJ and 8N-RP arestabilized by H-bonding interactions between the protonated amine and the $SnBr_6^{4-}$blocks. In the Fourier transform infrared (FTIR) spectra of 8N8-DJ and 8N-RP, the N-H stretching frequency is upshifted to 3386 cm^{-1} than 3318 cm^{-1} for the pristine non-protonated ligands (Figure S16). Likewise, the N-H bandsare downshifted than 3424 cm^{-1} for the pristine protonated ligands, implying the presence of H-bond with the $SnBr_6^{4-}$unit. 8N-RP contains 15 wt% Sn^{4+} having partial contribution from the secondary SnO phase, due to degradation of the 2D perovskite surface (Figure S15f and Table S4).[38]The binding energies of Br $3d_{5/2}$and Br $3d_{3/2}$ levels are less shifted from $SnBr_2$ than 8N8-DJ due to lower interaction between the organic and inorganic moieties (Figure S15g).Similarly, the lower fraction of protonated amine in 8N-RP than 8N8-DJ indicates the presence of more unreacted ligands.

8N-RP has a broad absorption tail in the visible region and a broad emission band centered at ~600 nm with ~140 nm FWHM and Stokes shift of ~160 nm at λ_{ex}= 360 nm (Figure 5c). Similar to the DJ phase, the PL intensity of 8N-RP increases with decreasing λ_{ex} (Figure 5d). 8N-RP also demonstrates a decent reversibility of the PL intensity over four cycles at different λ_{ex} from 320 to 420 nm, respectively (Figure S15h). The fresh 8N-RP demonstrates an excellent PLQY of 91.7±0.6% at λ_{ex} of 320 nm, which drops significantly at $\lambda_{ex} \geq$ 350 nm (Figure 5e). Here too, the temperature dependent PL spectra show the dominance of STE emission over the BE emission bands at a lower λ_{ex} of 360 nm (Figure S17), corroborating the high PLQY. At λ_{ex} of 380 nm, BE emission is more prominent from 5 to 125K, before the broad and intense STE emission overshadows above 175K.

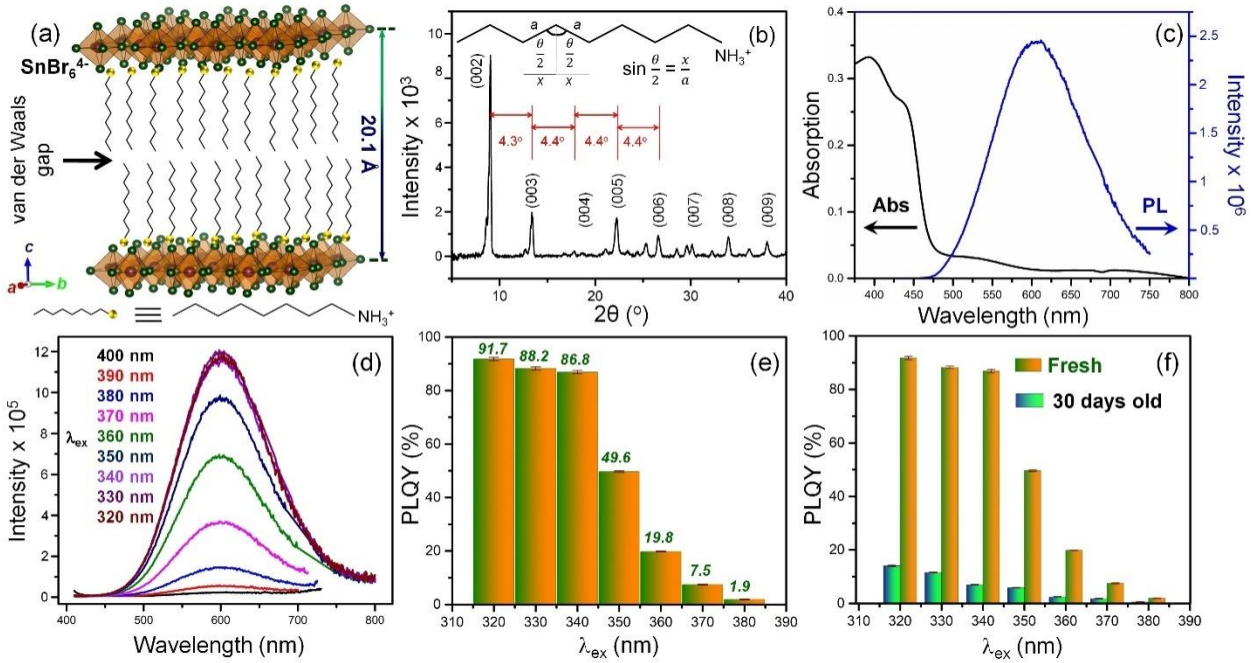

Figure 5. Structural and optical properties of 8N-RP powder. (a) Schematic crystal structure and (b) XRD pattern. Inset of (b) shows the *n*-octylamine ligand. (c) Absorption and PL emission spectra (λ_{ex} = 360 nm), and (d) λ_{ex} dependent PL spectra. (e) Bar plots of PLQY at different λ_{ex}. (f) Ambient-instability of PLQY shown by the bar plot comparison between the fresh and 30 days stored samples(under RH of 55% at 25°C) at different λ_{ex}.

8N8-DJ versus 8N-RP

The major advantage of 8N8-DJ over 8N-RP is the sustainability of its near-unity PLQY. As shown in Figure 5f, the PLQY of the 30 days old 8N-RP samplestored under RH of 55%, drops drastically at all λ_{ex}. Unlike 8N8-DJ, the absorbance, PLE and PL intensity (with λ_{ex} of 360 nm) of 8N-RP diminishes after the 30 days storage (Figure S15i and Figure S18a-c). Contrary to the pristine stability of 8N8-DJ, the 8N-RP phase partially degrades, as evident from the additional XRD reflections (Figure S18d). According to the XPS analysis, a secondary SnO phase emerges due to its gradual degradation. The digital images under visible and UV light show that while the 30 days old 8N8-DJ powder retains its PL property, the old 8N-RP powder loses the emissive nature (Figure S19). In addition, the lower compressive strain of the 8N8-DJ phase makes it a more rigid system than 8N-RP, leading to better stability of its optical properties at room temperature. The slopes of the Williamson-Hall plots show that 8N8-DJ has a lower lattice strain of 2.3×10^{-3} as compared to 5.4×10^{-3} for 8N-RP (Figure S13a and S20).[39]

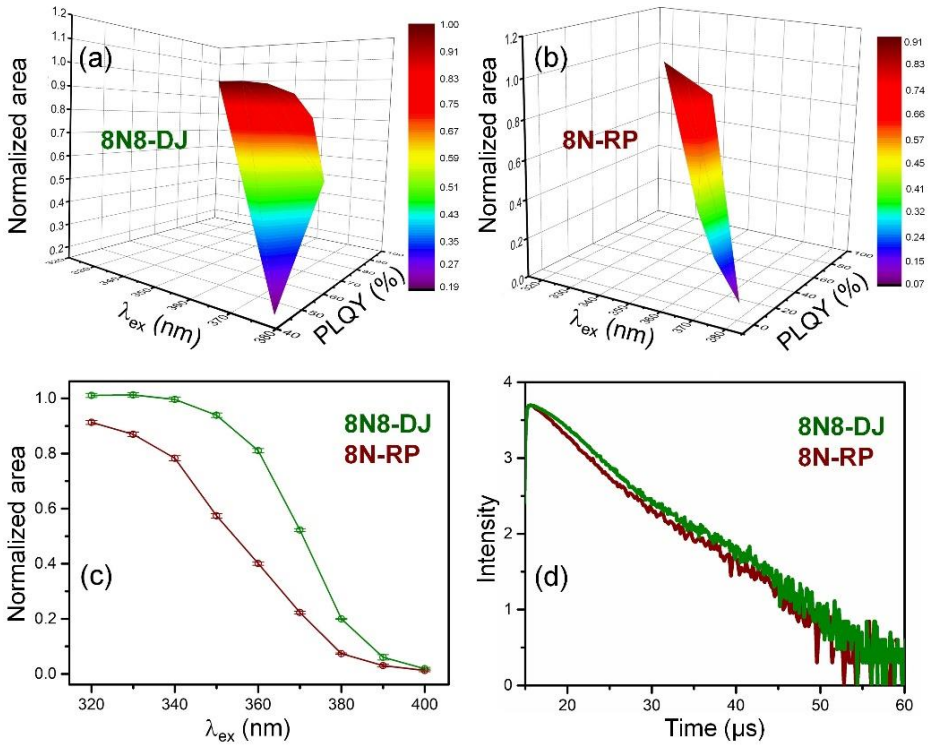

Figure 6. 3D contour plots of (a) 8N8-DJ and (b) 8N-RP perovskites in terms of normalized area of the room temperature PL spectra (primarily A_{STE}), λ_{ex} and PLQY. (c) Plot of normalized area of the room temperature PL spectra vs λ_{ex}, and (d) lifetime decay plots for 8N8-DJ and 8N-RP powders.

The 3D contour plots of PLQY vs λ_{ex} and the normalized area under the STE band summarize the results. The DJ and RP perovskites experience an increase in PLQY and the normalized area with decreasing λ_{ex}(Figure 6a,b). Here, the better emissive properties of 8N8-DJ can be understood from the higher integrated area under the PL curves over 8N-RP phase (Figure 6c). The STE emission being the origin of the near-unity PLQY for both the phases, the fitted lifetime decay plots show the biexponential components having average PL lifetime (τ_{ave}) greater than 2μs (Figure 6d and Table S5). 8N8-DJ has a marginally higher lifetime of the charge carriers than 8N-RP.

Stability of DJ perovskites with different spacers

Since the DJ perovskite exhibits better stability, a comparative stability test was conducted between the DJ perovskites having different spacer lengths in the presence of moisture (28°C and RH 75% for 3 days) and heat (100°C for 3 h). All the DJ perovskites retain strong emission features at 100°C for 3 h (Figure S21a-c), but the PL intensity decreases slightly

under the extreme humid conditions of RH 75% at 28°C for 3 days (Figure S21a-c). At RH 75%, the decrease in PL emission is the lowest in case of 8N8-DJ, which retains 91% of the initial intensity. The greater stability of 8N8-DJ perovskite is imparted by the more hydrophobic 8N8 spacer in between the inorganic layers, and therefore exhibits unchanged near unity PLQY in the presence of heat and moisture (Figure S21d and Table S6). Under similar conditions, the PLQY of 6N6-DJ is significantly affected. The PLQY of 8N8-DJ excels over the reported results of Sn-based layered perovskites (Table S7),[8-9,13,40-48] Pb-free organic-inorganic composites (Table S8),[29,49-52]and Pb-based layered perovskites (Table S9),[7,53-58]while that of the unstable 8N-RP perovskite is still comparable to the best reports.Our experimental results assert that 8N8-DJ is several notches above than the RP counterpart (8N-RP), the analogous 8N8$PbBr_4$ and the DJ perovskites with shorter spacer lengths, in terms of its PLQY and ambient stability.

Conclusions

In summary, we have introduced 1,8 diammonium octane spacercation in tin bromide perovskite to create a stable DJ phase (8N8-DJ) having near-unity PLQY of 99.7±0.3%. The emissive characteristics and PLQY remain unchanged when the 8N8-DJ powder is stored under ambient conditions of 25°C and RH of 55%for over one month. The RP perovskite with *n*-octylammonium spacer cation (8N-RP) also has extremely high PLQY of 91.7±0.6%, which on the contrary, becomes unsustainable due to more lattice strain and gradual degradation of the perovskite phase.In both the systems, the PLQY is correlated to the STE emission and remains constant at different λ_{ex}, especially below 360 nm.The 2D perovskite with ahydrophobic spacer chain length comprising of 8-carbon atoms (8N8-DJ) is found to be most suitable for obtaining the near-unity PLQY and pristine ambient stability in comparison to those with shorter chain length spacers (6N6-DJ and 4N4-DJ).While storage of these samples at 100°C for 3 h does not affect the strong emission features, the PL intensity of 6N6-DJ and 4N4-DJ decreases under the extreme humid conditions of RH 75% (stored 3 days), among which 8N8-DJ retains the maximum 91% of the initial PL intensity. A strong carrier-phonon coupling exists in 8N8-DJ at room temperature, which is characterized by the high Huang–Rhys factor (S) of 28.5±1.4and exciton-LO phonon coupling strength (γ_{LO}) of 195.0±1.3 meVat λ_{ex} = 360 nm. At λ_{ex}> 360 nm, BE emission becomes more prominent especially at temperatures below 75K, whereas STE emission intensity increases at higher temperatures. With increasing λ_{ex}, theγ_{LO} and

$\hbar\omega_{ph}$parameters decrease, which lowers the STE peak intensity as well as the PLQY.The 8N8-DJ (n = 1) perovskite powder not only demonstrates a near-unity PLQY over a wide λ_{ex}range, the PLQY also remains unchanged in the polymer-embedded films as well as after its storage for over one monthat RH of 55%.Owing to the outstanding sustainability of the near-unity PLQY, it is indubitable that 8N8-DJ has an extremely propitious prospect in future optoelectronics.

Experimental section

Chemicals and Materials:

Hydrobromic acid (HBr, 48 wt% in H_2O, Sigma Aldrich), Stannous bromide ($SnBr_2$, Sigma Aldrich), hypophosphorous acid (H_3PO_2, 50 wt% in H_2O, Spectrochem), *n*-octylamine ($C_8H_{17}NH_2$, 99%, Spectrochem), 1,8 diaminooctane ($NH_2C_8H_{16}NH_2$, TCI), hexane (Merck), diethyl ether ($C_2H_5OC_2H_5$) Merck) and chloroform ($CHCl_3$, Merck) were used without further purification.

Synthesis of $(NH_3C_8H_{16}NH_3)SnBr_4$(8N8-DJ): 0.36mM of $SnBr_2$ powder and 0.55 mM of 1,8 diaminooctane were dissolved in 1.5 ml concentrated HBr solution under vigorous stirring at 60^{o}C for 30 min, followed by the addition of 3 ml H_3PO_2 to prevent the oxidation of Sn^{2+} to Sn^{4+}. The mixture was allowed to stir at 100^{o}C for 30 min to form a colorless clear solution. After slow cooling, the yellow fluorescent solution of 8N8-DJ perovskite was obtained. The product was filtered accompanied by multiple washing with ether and chloroform.

*Synthesis of $(NH_3C_4H_8NH_3)SnBr_4$(4N4-DJ) and $(NH_3C_6H_{12}NH_3)SnBr_4$(6N6-DJ):*4N4-DJ and 6N6-DJ perovskites were synthesized by the same method asfor 8N8-DJ except instead of 1,8 diaminooctane, 0.55mM 1,4 diaminobutanewas used for 4N4-DJ, and 0.55mM 1,6 diaminobutanewas used to prepare 6N6-DJ. The process of filtration and purification steps were kept the same asper the procedure of 8N8-DJ.

Synthesis of $(C_8H_{17}NH_3)SnBr_4$ [8N-RP]: 0.36 mM $SnBr_2$ powder was dissolved in 1.5 ml concentrated HBr solution under vigorous stirring at 60^{o}C for 30 min, followed by the addition of 3 ml H_3PO_2. 190 µL of *n*-octylamine was added dropwise to the acidic solution of $SnBr_2$ followed by heating at 120^{o}C for 30 min to obtain the colorless clear solution. After slow cooling, the solution was filtered and washed with hexane several times to obtain the yellow colored and orange light-emitting 8N-RP perovskite.

*Preparation of 8N8-DJ perovskite films:*50 mg of 8N8-DJ powder and 25 mg PMMA binder were taken in three glass vials. Ethyl acetate was added in different proportions of 200, 400 and

600µL to prepare perovskite solutions having three different concentrations. The solutions were sonicated for 5 min to prepare the colloidal solutions: DJ-1 (250 mg/mL); DJ-2 (125 mg/mL) and DJ-3 (83 mg/mL). 100 µL of each solution wasdropcasted on 1 cm × 1 cm glass substrate and the films were dried. The process was repeated three times to prepare the perovskite films with different thicknesses.

Characterization: XRD measurements were performed with Rigaku X-ray diffractometer (Cu Kα irradiation, λ = 1.541 Å). The FESEM images were obtained in Carl Zeiss SUPRA 55VP FESEM. The EDX spectra and mapping were recorded in an Oxford Instruments X-Max system with the INCA software coupled to FESEM. TEM images were recorded with the DST-FIST facility, IISER Kolkata, JEOL, JEM-2100F. AFM images were taken with NT-MDT NTEGRA instrument from NT-MDT (Santa Clara, CA). FTIR spectral data was obtained with a PerkinElmer spectrum two spectrometer using KBr pellets.UV-vis absorption spectra of the solid samples were recorded by Jasco V-670 spectrophotometer and PL spectra were measured with Horiba Jobin Yvon Fluorolog using Xe lamp as the excitation source. PL spectra of all the samples at room temperature were taken by preparing a solid film of the samples by using a solid-state PL holder. Absolute quantum yield was measured in FLS-1000 Edinburgh with an Integrating sphere setup. The lamp source was Xe-400, and the detector was PMT-400 and PMT-400+ integrating sphere.

Calculation of lattice strain:

The intrinsic strain of 8N8-DJ and 8N-RP perovskites were calculated by the Williamson-Hall equation (7):

$$\beta_{hkl} \cos\theta = \frac{k\lambda}{D + 4\epsilon \sin\theta} \quad (7)$$

where β_{hkl} is FWHM of the XRD peak, k is the Scherrer constant, λ is the wavelength of X-ray radiation, D is the crystallite size and ε is the strain. The ε values were determined from the slope of $\beta_{hkl}cos\theta$ versus $4\varepsilon sin\theta$ plots.

Calculation of average lifetime:

The PL decay profile was performed using time-correlated single-photon counting (TCSPC) method with FLS-1000 Edinburgh instrument. The time-resolved PL decay curves were fitted by biexponential decay kinetics. The average PL lifetimes (τ_{ave}) were calculated from equations (8) and (9):

$$A(t) = A_1 e^{-\frac{t}{\tau 1}} + A_2 e^{-\frac{t}{\tau 2}} \quad (8)$$

$$\tau = \frac{(A_1 {\tau_1}^2 + A_2 {\tau_2}^2)}{(A_1 \tau_1 + A_2 \tau_2)} \quad (9)$$

Here, A_1 and A_2 denote the contributions of τ_1 and τ_2 components, respectively.

Low-temperature PL analysis of the perovskite films:

To perform the low-temperature PL measurements, the 8N8-DJ and 8N-RP perovskite films were prepared by dispersing the powders in chloroform by sonication, followed by drop-casting the dispersions on the top of sapphire substrate. Low-temperature PL experiments were carried out by using the second harmonic of a laser light from a mode-locked Ti: sapphire laser (Tsunami, Spectra-Physics), giving ~140 fs pulses at a repetition rate of 80 MHz, focused on the sample. The sample on the sapphire substrate was mounted in a closed cycle He-cryostat. The emitted luminescence was collected by a lens and then focused in a high-resolution grating spectrometer (Acton SP-25, Princeton Instruments) fitted with a Peltier-cooled 1340 × 100 CCD array detector, 20 × 20 μm^2 2-pixel size (PIXIS:100BR, Princeton Instruments). This CCD records the luminescence spectra. The temperature dependence study was performed after reaching 4K in a cryostat with a heater controlled by the temperature controller. The excitation wavelength was tuned by tuning the wavelength of Ti: sapphire laser. The excitation light intensity was controlled by a neutral-density filter.

Conflicts of Interest

There are no conflicts of interest to declare.

Supporting Information

AFM, SEM and TEM images; elementary mapping; XPS results; UV and PLE stability; low temperature PL experimental setup; temperature dependent PL spectra and PL peak energy plots; exciton binding energy; FWHM analysis; 8N-RP PL reversibility; FTIR spectra; XRD stability test; digital images; PL lifetime;PL and PLQY stability; comparison tables.

Acknowledgements

Ar.M. thanks University Grants Commission (UGC), New Delhi, S.R. thanks the INSPIRE fellowship from SERB, New Delhi andAn.M. acknowledges Council of Scientific and Industrial Research (CSIR), New Delhi. The financial support from SERB under Sanction No. CRG/2020/000084 and STR/2021/000001 are duly acknowledged.

References

(1) Xu, W.; Hu, Q.; Bai, S.; Bao, C.; Miao, Y.; Yuan, Z.; Borzda, T.; Barker, A. J.; Tyukalova, E.; Hu, Z.; Kawecki, M.; Wang, H.; Yan, Z.; Liu, X.; Shi, X.; Uvdal, K.; Fahlman, M.; Zhang, W.; Duchamp, M.; Liu, J.-M.; Petrozza, A.; Wang, J.; Liu, L.-M.; Huang, W.; Gao, F. Rational Molecular Passivation for High-Performance Perovskite Light-Emitting Diodes. *Nat. Photon*. **2019**, *13*, 418-424.

(2) Zhang, N.; Fan, Y.; Wang, K.; Gu, Z.; Wang, Y.; Ge, L.; Xiao, S.; Song, Q. All-Optical Control of Lead Halide Perovskite Microlasers. *Nat. Commun*. **2019**, *10*, 1770.

(3) Mandal, A.; Ghosh, A.; Ghosh, D.; Bhattacharyya, S. Photodetectors with High Responsivity by Thickness Tunable Mixed Halide Perovskite Nanosheets. *ACS Appl. Mater. Interfaces* **2021**, *13*, 43104-43114.

(4) Ghosh, D.; Chaudhary, D.; Ali, M.; Chauhan, K.; Prodhan, S.; Bhattacharya, S.; Ghosh, B.; Datta, P.; Ray, S.; Bhattacharyya, S. All-Inorganic Quantum Dot Assisted Enhanced Charge Extraction Across the Interfaces of Bulk Organo-Halide Perovskites for Efficient and Stable Pin-Hole Free Perovskite Solar Cells. *Chem. Sci.* **2019**, *10*, 9530-9541.

(5) Dutta, A.; Behera, R. K.; Pal, P.; Baitalik, S.; Pradhan, N. Near-Unity Photoluminescence Quantum Efficiency for All $CsPbX_3$ (X = Cl, Br, and I) Perovskite Nanocrystals: A Generic Synthesis Approach. *Angew. Chem. Int. Ed*. **2019**, *58*, 5552-5556.

(6) Li, X.; Hoffman, J. M.; Kanatzidis, M. G. The 2D Halide Perovskite Rulebook: How the Spacer Influences Everything from the Structure to Optoelectronic Device Efficiency. *Chem. Rev*. **2021**, *121*, 2230-2291.

(7) Na Quan, L.; Ma, D.; Zhao, Y.; Voznyy, O.; Yuan, H.; Bladt, E.; Pan, J.; García de Arquer, F.; Sabatini, R.; Piontkowski, Z. et al. Edge Stabilization in Reduced-Dimensional Perovskites. *Nat. Commun.* **2020**, *11*,170.

(8) Zhang, X.; Wang, C.; Zhang, Y.; Zhang, X.; Wang, S.; Lu, M.; Cui, H.; Kershaw, S.; Yu, W.; Rogach, A. Bright Orange Electroluminescence from Lead-Free Two-Dimensional Perovskites. *ACS Energy Lett.* **2018**, *4*, 242-248.

(9) Cao, J.; Guo, Z.; Zhu, S.; Fu, Y.; Zhang, H.; Wang, Q.; Gu, Z. Preparation of Lead-Free Two-Dimensional-Layered $(C_8H_{17}NH_3)_2SnBr_4$ Perovskite Scintillators and Their Application in X-Ray Imaging. *ACS Appl. Mater. Interfaces* **2020**, *12*, 19797-19804.

(10) Liu, Y.; Wang, A.; Wu, J.; Wang, C.; Li, Z.; Hu, G.; Sui, S.; She, J.; Meng, W.; Li, W.; Deng, Z. Alkylamine Screening and Zinc Doping of Highly Luminescent 2D Tin-Halide Perovskites for LED Lighting. *Mater. Adv.* **2021**, *2*, 1320-1327.

(11) Li, Z.; Deng, Z.; Johnston, A.; Luo, J.; Chen, H.; Dong, Y.; Sabatini, R.; Sargent, E. Precursor Tailoring Enables Alkylammonium Tin Halide Perovskite Phosphors for Solid-State Lighting. *Adv. Funct. Mater.* **2022**, *32*, 2111346.

(12) Liu, Y.; Deng, Z. Fast Synthesis of Highly Luminescent Two-dimensional Tin-halide Perovskites by Anti-Solvent Method. *Chem. J. Chin. Univ.* **2021**, *42*, *12*, 3774-3782.

(13) Wang, S.; Popović, J.; Burazer, S.; Portniagin, A.; Liu, F.; Low, K.; Duan, Z.; Li, Y.; Xiong, Y.; Zhu, Y.; Kershaw, S.; Djurišić, A.; Rogach, A. Strongly Luminescent Dion–Jacobson Tin Bromide Perovskite Microcrystals Induced by Molecular Proton Donors Chloroform and Dichloromethane. *Adv. Func. Mater.***2021**, *31*, 2102182.

(14) Hassan, Y.; Song, Y.; Pensack, R.; Abdelrahman, A.; Kobayashi, Y.; Winnik, M.; Scholes, G. Structure-Tuned Lead Halide Perovskite Nanocrystals. *Adv. Mater.* **2015**, *28*, 566-573.

(15) Biswas, A.; Bakthavatsalam, R.; Kundu, J. Efficient Exciton to Dopant Energy Transfer in Mn^{2+}-Doped $(C_4H_9NH_3)_2PbBr_4$ Two-Dimensional (2D) Layered Perovskites. *Chem. Mater.* **2017**, *29*, 7816-7825.
(16) Lanzetta, L.; Marin-Beloqui, J.; Sanchez-Molina, I.; Ding, D.; Haque, S. Two-Dimensional Organic Tin Halide Perovskites with Tunable Visible Emission and their Use in Light-Emitting Devices. *ACS Energy Lett.* **2017**, *2*, 1662-1668.
(17) Zhou, C.; Tian, Y.; Wang, M.; Rose, A.; Besara, T.; Doyle, N.; Yuan, Z.; Wang, J.; Clark, R.; Hu, Y.; Siegrist, T.; Lin, S.; Ma, B. Low-Dimensional Organic Tin Bromide Perovskites And Their Photoinduced Structural Transformation. *Angew. Chem. Int. Ed.* **2017**, *129*, 9146-9150.
(18) Ahmad, S.; Fu, P.; Yu, S.; Yang, Q.; Liu, X.; Wang, X.; Wang, X.; Guo, X.; Li, C. Dion-Jacobson Phase 2D Layered Perovskites for Solar Cells with Ultrahigh Stability. *Joule* **2019**, *3*, 794-806.
(19) Mao, L.; Ke, W.; Pedesseau, L.; Wu, Y.; Katan, C.; Even, J.; Wasielewski, M.; Stoumpos, C.; Kanatzidis, M. Hybrid Dion-Jacobson 2D Lead Iodide Perovskites. *J. Am. Chem. Soc.* **2018**, *140*, 3775-3783.
(20) Shang, Y.; Liao, Y.; Wei, Q.; Wang, Z.; Xiang, B.; Ke, Y.; Liu, W.; Ning, Z. Highly Stable Hybrid Perovskite Light-Emitting Diodes Based on Dion-Jacobson Structure. *Sci.Adv.* **2019**, *5*, eaaw8072.
(21) Travis, W.; Glover, E.; Bronstein, H.; Scanlon, D.; Palgrave, R. On The Application of the Tolerance Factor to Inorganic and Hybrid Halide Perovskites: A Revised System. *Chem. Sci.* **2016**, *7*, 4548-4556.
(22) Stoumpos, C.; Malliakas, C.; Kanatzidis, M. Semiconducting Tin and Lead Iodide Perovskites with Organic Cations: Phase Transitions, High Mobilities, and Near-Infrared Photoluminescent Properties. *Inorg. Chem.* **2013**, *52*, 9019-9038.
(23) Xu, L.; Lin, H.; Lee, S.; Zhou, C.; Worku, M.; Chaaban, M.; He, Q.; Plaviak, A.; Lin, X.; Chen, B.; Du, M.; Ma, B. 0D and 2D: The Cases of Phenylethylammonium Tin Bromide Hybrids. *Chem. Mater.* **2020**, *32*, 4692-4698.
(24) Huang, P.; Kazim, S.; Wang, M.; Ahmad, S. Toward Phase Stability: Dion–Jacobson Layered Perovskite for Solar Cells. *ACS Energy Lett.* **2019**, *4*, 2960-2974.
(25) Wang, S.; Kershaw, V.; Rogach, A. Bright and Stable Dion-Jacobson Tin Bromide Perovskite Microcrystals Realized by Primary Alcohol Dopants. *Chem. Mater.* **2021**, *33*, 5413-5421.
(26) Zhang, L.;Yang, B.; Mei, S.; Zhu, Y.; Hu, R.; Zou, J. Highly Luminescent Broadband Phosphors Based on Acid Solvent Co-ordinated Two-dimensional Layered Tin-based Perovskites. *J. Mater. Chem. C* **2022**, *10*, 3856-3862.
(27) Ghosh, A.; Chaudhary, D.; Mandal, A.; Prodhan, S.; Chauhan, K.; Vihari, S.; Gupta, G.; Datta, P.; Bhattacharyya, S. Core/Shell Nanocrystal Tailored Carrier Dynamics in Hysteresis-less Perovskite Solar Cells with ∼20% Efficiency and Long Operational Stability. *J. Phys. Chem. Lett.* **2020**, *11*, 591-600.
(28) Shi, Y.; Zhao, W.; Ma, Z.; Xiao, G.; Zou, B. Self-trapped Exciton Emission and Piezochromism in Conventional 3D Lead Bromide Perovskite Nanocrystals Under High Pressure. *Chem. Sci*. **2021**, *12*, 14711-14717.
(29) Wei, Q.; Chang, T.; Zeng, R.; Cao, S.; Zhao, J.; Han, X.; Wang, L.; Zou, B. Self-Trapped Exciton Emission in a Zero-Dimensional $(TMA)_2SbCl_5{\cdot}DMF$ Single Crystal and Molecular Dynamics Simulation of Structural Stability. *J. Phys. Chem. Lett.* **2021**, *12*, 7091-7099.

(30) Laxmi; Kabra, D. Origin of Contrasting Emission Spectrum of Bromide Versus Iodide Layered Perovskite Semiconductors. *J. Phys. Chem. Lett.* **2022**, *13*, 2737-2743.
(31) Hu, T.; Smith, M.; Dohner, E.; Sher, M.; Wu, X.; Trinh, M.; Fisher, A.; Corbett, J.; Zhu, X.; Karunadasa, H.; Lindenberg, A. Mechanism for Broadband White-Light Emission from Two-Dimensional (110) Hybrid Perovskites. *J. Phys. Chem. Lett.* **2016**, *7*, 2258-2263.
(32) Ai, B.; Liu, C.; Deng, Z.; Wang, J.; Han, J; Zhao, X. Low Temperature Photoluminescence Properties of $CsPbBr_3$ Quantum Dots Embedded in Glasses. *Phys. Chem. Chem. Phys.* **2017**,*19*, 17349-17355.
(33) Wu, K.;Bera, A.; Ma, C.; Du, Y.; Yang, Y.; Li, L.; Wu, T. Temperature-Dependent Excitonic Photoluminescence of Hybrid Organometal Halide Perovskite Films. *Phys. Chem. Chem. Phys.* **2014**, *16*, 22476-22481.
(34) Liang, M.; Lin, W.; Zhao, Q.; Zou, X.; Lan, Z.; Meng, J.; Shi, Q.; Castelli, I.; Canton, S.; Pullerits, T.; Zheng, K. Free Carriers Versus Self-Trapped Excitons at Different Facets of Ruddlesden–Popper Two-Dimensional Lead Halide Perovskite Single Crystals. *J. Phys. Chem. Lett.* **2021**, *12*, 4965-4971.
(35) Smith, M.; Karunadasa, H. White Light Emission from Layered Halide Perovskites. *Acc. Chem. Res.***2018**, *51*, 619-627.
(36) Smith, M.; Jaffe, A.; Dohner, E.; Lindenberg, A.; Karunadasa, H. Structural Origins of Broadband Emission from Layered Pb–Br Hybrid Perovskites. *Chem.Sci.* **2017**, *8*, 4497-4504.
(37) Deng, C.; Zhou, G.; Chen, D.; Zhao, J.; Wang, Y.; Liu, Q. Broadband Photoluminescence in 2D Organic–Inorganic Hybrid Perovskites: $(C_7H_{18}N_2)PbBr_4$ and $(C_9H_{22}N_2)PbBr_4$. *J.Phys. Chem. Lett.* **2020**, *11*, 2934-2940.
(38) Stranick, M.; Moskwa, A. SnO by XPS. *Surf. Sci. Spectra* **1993**, *2*, 45-49.
(39) Mandal, A.; Ghosh, A.; Senanayak, S.; Friend, R.; Bhattacharyya, S. Thickness-Attuned $CsPbBr_3$ Nanosheets with Enhanced P-Type Field-Effect Mobility. *J. Phys. Chem. Lett.* **2021**, *12*, 1560-1566.
(40) Qi, J.; Wang, S.; Portniagin, A.; Kershaw, S.; Rogach, A. Room-Temperature Fabrication of Stable, Strongly Luminescent Dion–Jacobson Tin Bromide Perovskite Microcrystals Achieved Through Use of Primary Alcohols. *Nanomaterials* **2021**, *11*, 2738.
(41) Wang, S.; Kershaw, S.; Rogach, A. Bright and Stable Dion-Jacobson Tin Bromide Perovskite Microcrystals Realized by Primary Alcohol Dopants. *Chem.Mater.* **2021**, *33*, 5413-5421.
(42) Wang, A.; Guo, Y.; Zhou, Z.; Niu, X.; Wang, Y.; Muhammad, F.; Li, H.; Zhang, T.; Wang, J.; Nie, S.; Deng, Z. Aqueous Acid-Based Synthesis of Lead-Free Tin Halide Perovskites with Near-Unity Photoluminescence Quantum Efficiency. *Chem. Sci.***2019**, *10*, 4573-4579.
(43) Zhou, C.; Tian, Y.; Yuan, Z.; Lin, H.; Chen, B.; Clark, R.; Dilbeck, T.; Zhou, Y.; Hurley, J.; Neu, J.; Besara, T.; Siegrist, T.; Djurovich, P.; Ma, B. Highly Efficient Broadband Yellow Phosphor Based on Zero-Dimensional Tin Mixed-Halide Perovskite. *ACS Appl. Mater. Interfaces* **2017**, *9*, 44579-44583.
(44) Zhou, C.; Lin, H.; Shi, H.; Tian, Y.; Pak, C.; Shatruk, M.; Zhou, Y.; Djurovich, P.; Du, M.; Ma, B. A Zero-Dimensional Organic Seesaw-Shaped Tin Bromide with Highly Efficient Strongly Stokes-Shifted Red Emission. *Angew.Chem.Int.Ed.***2018**,*57*,1021–1024.
(45) Su, B.; Song, G.; Molokeev, M.; Lin, Z.; Xia, Z. Synthesis, Crystal Structure and Green Luminescence in Zero-Dimensional Tin Halide $(C_8H_{14}N_2)_2SnBr_6$. *Inorg. Chem.* **2020**, *59*, 9962-9968.

(46) Spanopoulos, I.; Hadar, I.; Ke, W.; Guo, P.; Sidhik, S.; Kepenekian, M.; Even, J.; Mohite, A.; Schaller, R.; Kanatzidis, M. Water-Stable 1D Hybrid Tin(II) Iodide Emits Broad Light with 36% Photoluminescence Quantum Efficiency. *J. Am. Chem. Soc.* **2020**, *142*, 9028-9038.
(47) Zhou, C.; Lin, H.; Tian, Y.; Yuan, Z.; Clark, R.; Chen, B.; van de Burgt, L.; Wang, J.; Zhou, Y.; Hanson, K.; Meisner, Q.; Neu, J.; Besara, T.; Siegrist, T.; Lambers, E.; Djurovich, P.; Ma, B. Luminescent Zero-Dimensional Organic Metal Halide Hybrids with Near-Unity Quantum Efficiency. *Chem. Sci.* **2018**, *9*, 586-593.
(48) Morad, V.; Shynkarenko, Y.; Yakunin, S.; Brumberg, A.; Schaller, R.; Kovalenko, M. Disphenoidal Zero-Dimensional Lead, Tin, and Germanium Halides: Highly Emissive Singlet and Triplet Self-Trapped Excitons and X-Ray Scintillation. *J. Am. Chem. Soc.* **2019**, *141*, 9764-9768.
(49) Zhou, L.; Liao, J.; Huang, Z.; Wei, J.; Wang, X.; Chen, H.; Kuang, D. Intrinsic Self-Trapped Emission In 0D Lead free $(C_4H_{14}N_2)_2In_2Br_{10}$ Single Crystal. *Angew. Chem.Int. Ed.***2019**, *131*, 15581-15586.
(50) Li, Z.; Li, Y.; Liang, P.; Zhou, T.; Wang, L.; Xie, R.-J. Dual-Band Luminescent Lead-Free Antimony Chloride Halides with Near-Unity Photoluminescence Quantum Efficiency. *Chem. Mater.* **2019**, *31*, 9363-9371.
(51) Zhou, C.; Worku, M.; Neu, J.; Lin, H.; Tian, Y.; Lee, S.; Zhou, Y.; Han, D.; Chen, S.; Hao, A.; Djurovich, P.; Siegrist, T.; Du, M.; Ma, B. Facile Preparation of Light Emitting Organic Metal Halide Crystals with Near-Unity Quantum Efficiency. *Chem. Mater.* **2018**, *30*, 2374-2378.
(52) Peng, H.; Tian, Y.; Yu, Z.; Wang, X.; Ke, B.; Zhao, Y.; Dong, T.; Wang, J.; Zou, B. $(C_{16}H_{28}N)_2SbCl_5$: A New Lead-Free Zero-Dimensional Metal-Halide Hybrid with Bright Orange Emission. *Sci. China Mater.* **2022**, *65*, 1594-1600.
(53) Xing, G.; Wu, B.; Wu, X.; Li, M.; Du, B.; Wei, Q.; Guo, J.; Yeow, E.; Sum, T.; Huang, W. Transcending the Slow Bimolecular Recombination in Lead-Halide Perovskites for Electroluminescence. *Nat. Commun.* **2017**, *8*,14558.
(54) La-Placa, M.; Longo, G.; Babaei, A.; Martínez-Sarti, L.; Sessolo, M.; Bolink, H. Photoluminescence Quantum Yield Exceeding 80% in Low Dimensional Perovskite Thin-Films via Passivation Control. *Chem. Commun.* **2017**, *53*, 8707-8710.
(55) Biswas, A.; Bakthavatsalam, R.; Shaikh, S.; Shinde, A.; Lohar, A.; Jena, S.; Gonnade, R.; Kundu, J. Efficient Broad-Band Emission from Contorted Purely Corner-Shared One Dimensional (1D) Organic Lead Halide Perovskite. *Chem. Mater.* **2019**, *31*, 2253-2257.
(56) Yang, S.; Niu, W.; Wang, A.; Fan, Z.; Chen, B.; Tan, C.; Lu, Q.; Zhang, H. Ultrathin Two-Dimensional Organic-Inorganic Hybrid Perovskite Nanosheets with Bright, Tunable Photoluminescence and High Stability. *Angew. Chem. Int. Ed.* **2017**, *129*, 4316-4319.
(57) Yang, X.; Zhang, X.; Deng, J.; Chu, Z.; Jiang, Q.; Meng, J.; Wang, P.; Zhang, L.; Yin, Z.; You, J. Efficient Green Light-Emitting Diodes Based On Quasi-Two-Dimensional Composition and Phase Engineered Perovskite with Surface Passivation. *Nat. Commun.* **2018**, *9*,570.
(58) Dohner, E.; Jaffe, A.; Bradshaw, L.; Karunadasa, H. Intrinsic White-Light Emission from Layered Hybrid Perovskites. *J. Am. Chem. Soc.* **2014**, *136*, 13154-13157.

Table of Contents